© Universiti Tun Hussein Onn Malaysia Publisher's Office

EmAIT

Journal homepage: http://publisher.uthm.edu.my/ojs/index.php/emait
e-ISSN : 2773-5540

Emerging Advances in Integrated Technology

Fabrication of A Diode-based Salt Solution Sensor

Li Fang Lai[1,2], Nurfarina Zainal[1,2], Chin Fhong Soon[1,2*]

[1]Department of Electronic Engineering, Faculty of Electrical & Electronic,
Universiti Tun Hussein Onn Malaysia, 86400, Parit Raja, Batu Pahat, Johor, MALAYSIA

[2]Microelectronics and Nanotechnology-Shamsuddin Research Centre (MiNT-SRC),
Universiti Tun Hussein Onn Malaysia, Parit Raja, Batu Pahat, Johor, MALAYSIA

*Corresponding Author

DOI: https://doi.org/10.30880/emait.2020.01.01.002
Received 17 September 2020; Accepted 01 October 2020; Available online 01 November 2020

Abstract: High blood pressure/hypertension is a severe medical issue among Malaysians that could be reduced by monitoring our salt/sodium intake. One way is to use intraoral salt sensor; this in-mouth method however may cause discomfort and adopts complex and costly fabrication processes. Hence, an external and reusable electronic device, that could be used as a "sweat-sensor", is preferred in detecting the sodium intake of the body. In this study, a potentiometric diode-based salt solution sensor was designed and fabricated in order to detect different salt solution concentrations with applied external voltage. A *p-n* junction diode sensor was successfully designed and fabricated using four consecutive techniques; thermal wet oxidation, photolithography, thermal diffusion and metallization. The average sheet resistance and resistivity of the diode sensor were measured to be $3.50 \times 10^5 \pm 0.66$ Ω/sq and 3.05 ± 0.5 Ωcm respectively. This sensor showed ideal I-V diode characteristics with a knee voltage of 11.5V in forward bias condition and breakdown voltage of -4 V in reverse bias condition. For salt concentration detection, the sensor was able to detect salt concentration changes with respect to current flow, up to 45 mg/mL.

Keywords: Diode, sensor, *p-n* junction, fabrication, salt solution, I-V measurement

1. Introduction

Studies have shown adverse effects of salt intake in humans, especially high blood pressure. Excess consumption of salt or sodium (>5 g per day) will significantly increase our blood pressure, which has been linked to various cardiovascular complications [1]. To date, researchers have found ways in developing electrochemical sensors that could detect analyte levels (e.g. glucose, lactate) *via* bodily fluids such as saliva or sweat. [2]- [10]. Arakawa *et al.* developed detachable "*Cavitas* sensors" to apply to human oral cavity to monitor glucose concentration in saliva [8], while Kim *et al.* presented the works of non-invasive mouthguard biosensors for salivary monitoring of metabolites [9] and uric acid [10]. These intraoral sensors however are held in rigid plastic boards and may cause discomfort to users by excessive mechanical and thermal loading [11].

Non-invasive wearable sensors for sweat detection have also been extensively studied. Sweat or perspiration is essential for physiological function in humans; the body regulates homeostasis and hydrates through the sweat glands in the skin. [12] The composition of sweat is mainly water, minerals (i.e. sodium, potassium, calcium) and metabolites (i.e. ammonia, urea). Recently, Pirovano *et al.* improved the SwEatch platform, a device that samples and measures the concentration of sodium Na^+ and potassium K^+ in human sweat. They fabricated poly(3,4-ethylene-dioxythiophene) (PEDOT)-based Na^+ and K^+ ion selective electrodes, which generated a new set of real-time data for measuring electrolytes in sweat in athletes [2]. Hence, in this paper, a new type of salt sensor is designed and fabricated; a diode-based sensor that can detect different concentrations of salt solution. This diode has a planar design and adopted *p-n* junction as the sensing part.

*Corresponding author: soon@uthm.edu.my

2020 UTHM Publisher. All rights reserved.

1.1 *P-n* Junction Diodes

A diode is a two-electrode device, which consists of an anode and a cathode. A key component of a diode is a junction which allows current flow of one direction, but not in reverse [13]. Figure 1(a) shows the current flow from anode to cathode, when the anode voltage is positive with respect to cathode voltage. Most common diodes are based on *p-n* homo- or heterojunctions. Shown in Figure 1(b), a *p-n* junction diode is made up of two sides; one side is a *p*-type material with high concentration of positive holes, while the other is an *n*-type material with high concentration of negative electrons [14]. The transition zone between these two materials is known as the 'carrier depletion layer', and due to the high concentrations of positive holes and negative electrons on either side, a potential difference exists across this layer [15].

When an electric field is applied, two types of current will flow, known as diffusion current and drift current. Diffusion current is the majority carrier movement, and involves the movement of holes from *p* to *n* and electrons from *n* to *p*. Drift current is the opposite; holes instead move from *n* to *p* and electrons from *p* to *n*, and is the minority carrier movement. Shown in Figure 1(c), two situations can occur based on how the field is applied; by applying forward bias or reverse bias mode. In forward bias mode, the potential barrier is reduced and results in large diffusion current flow, the overall current is positive and large. In reverse bias mode, the potential barrier is increased and less diffusion current flow, the overall current is negative and very small [15]. When no bias is applied, there is no current flow, and the diffusion and drift currents that flow will cancel each other [16]. These basic semiconductor diodes characteristics display typical current-voltage or I-V relationship, depicted in Figure 1(c). Knee (or forward) voltage is the amount of voltage needed to get current to flow across the diode, while breakdown voltage is the amount of negative voltage needed to overcome the potential layer [17].

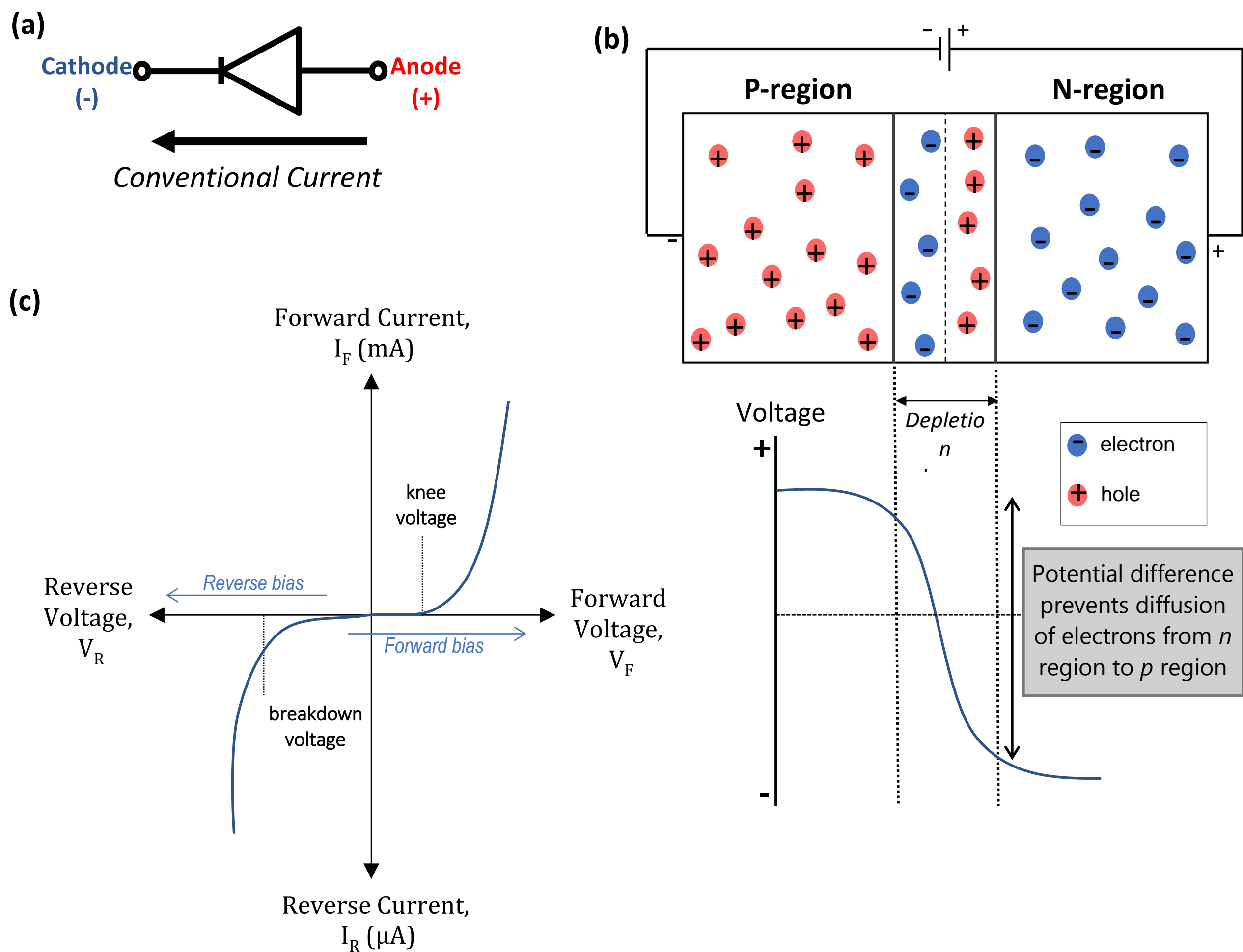

Fig. 1 - (a) current flow in diode, from anode to cathode; (b) *p-n* junction of a diode during reverse bias, a depletion layer is formed during this condition; (c) current-voltage (I-V) measurement of an ideal diode

1.2 Potentiometric Sensors

Potentiometric sensors are established as an analytical technology that has been extensively applied for physiological testing of key electrolytes [18]. These sensors measure the accumulation of a charge potential at the working (or indicator) electrode in an electrochemical cell, with no current flowing between the electrodes [19]-[20]. The type of electrodes used are known as ion-selective electrodes (ISE) [21]. The most common example of a potentiometric sensor is a pH meter, and the ISEs are commonly utilized for the determinations of ions such as sodium (Na^+), potassium (K^+), chloride (Cl^-), and ammonium (NH_4^+) ions [19].

All solid-state microsensors are potentiometric sensors that detect ions or conductive chemicals through a sensitive layer [22]. Figure 2 shows the planar configurations of potentiometric sensors with a chemically inert substrate, which undergo fabrication processes such as thin film deposition and metallization. In this study, a planar-based potentiometric diode sensor was fabricated.

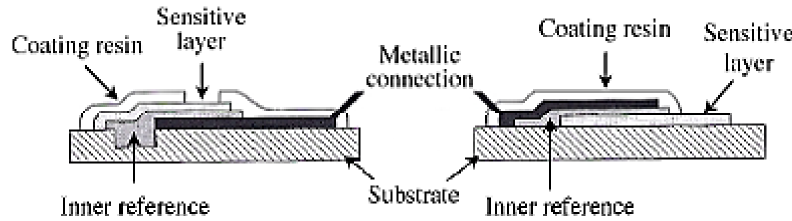

Fig. 2 - Two typical planar configurations for the elaboration of a potentiometric microsensor [22]

1.3 Electrical Characterization of Diodes

Electrical characterization of semiconductor diode has been an important subject at all time. Most common characterization includes current-voltage (I-V) measurements, sheet resistance and resistivity. In this study, two methods were used; two-point probe for I-V measurements, and four-point probe for average sheet resistance and resistivity of the diodes.

For the two-point probe method, two electrodes serve as both current and voltage sensing probes, shown in Figure 3(a) [23]. This method is typically used to measure resistivity of a material, but can also be used for I-V measurements. Application of voltage into the material will cause current to flow through the material. However, two-point probe is often not reliable for electrical measurements since there is usually some resistance between the contact wires and the material, or even in the measuring equipment [24]. This will cause the resistivity value of the material to appear higher than normal.

The four-point probe method is commonly used to measure electrical conductivity and is often preferred than the two-point probe [25]. A typical measurement involves the use of four tungsten carbide needles, arranged along a straight line with equal spacing, attached to the sample material, shown in Figure 3(b). A current source forces a constant electrical current I through the external needles, and the current is measured by an ammeter. A voltmeter simultaneously measures the voltage V produced between the inner needles. Once these parameters are obtained, the resistivity ρ and the sheet resistance R_{sh} of the material can be calculated using equations (1) and (2);

$$R_{sh} = \frac{\rho}{t} \qquad \Omega/\text{sq} \tag{1}$$

$$\rho = \frac{V}{I} \times 2\pi s \qquad \Omega\text{-cm} \tag{2}$$

ρ is the resistivity of the sample in Ω-cm, V is the DC voltage across the probes in volts, I is the constant DC current passing through the current probes in amperes, s is the spacing between the probes, R_{sh} is the sheet resistant and t is the sample thickness [25].

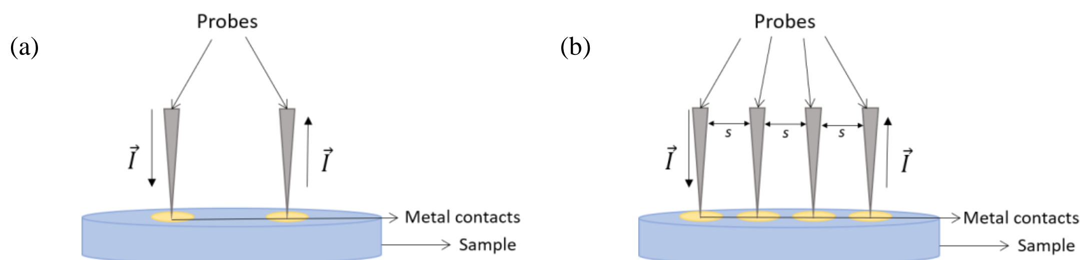

Fig. 3 - (a) Two-point probe method; (b) Four-point probe method

1.4 Fabrication of Diodes

Nowadays, the advancement of fabrication technology has reached an extensively high level of three-dimensional (3D) structure fabrication. However, planar technology is still preferred in integrated circuit fabrication, especially in semiconductor fabrication processes. The planar process includes four major steps; thermal oxidation, photolithography, thermal diffusion and metallization [26]. The overall process of a typical *p-n* junction diode is shown in Figure 4.

An *n*-type silicon wafer is typically used as the substrate, and prior to fabrication the wafer must be properly cleaned to remove any chemical contaminants and particulate impurities that will affect device performance [27]. Bare wafers can be cleaned using organic solvents such as isopropanol (IPA) and acetone. Then, thermal oxidation of the wafers will yield silicon dioxide (SiO_2). SiO_2 typically functions as an insulator, while in diodes SiO_2 film defines the junction area. There are two types of SiO_2 growth methods; dry and wet oxidation that depends on whether dry oxygen or water vapour is used. After oxidation, SiO_2 layer will be formed on the surface of the silicon wafer [26].

Next is the photolithography process. The wafer will be coated with a layer of photoresist, which is an ultra-violet (UV) light-sensitive material. The photoresist is spun on the wafer surface by a high-speed spinner, and then baked at around 80 – 100 ^{0}C to harden and remove all solvent for improved adhesion. A patterned mask is then placed on the wafer and is exposed with a UV light source; the exposed region of the wafer will be polymerized, and this region will stay in place when the wafer is placed in a developer, while the non-exposed region will dissolve and be washed away. The wafer is baked again at 120 – 150 ^{0}C for 20 minutes, then a hydrofluoric acid (HF) etchant is used to remove the unprotected SiO_2 surface. Finally, the photoresist is removed by using a chemical solution or oxygen plasma [26].

After photolithography, the wafer undergoes thermal diffusion or ion implantation, where the silicon surface not covered with oxide is exposed to a high concentration of opposite-type impurity (in this case, *p*-type). The SiO_2 layer acta as a barrier against the impurity, and after this process the *p-n* junction is formed. The width of *p*-region is slightly wider than the window opening due to lateral diffusion of the impurities [26].

Finally, a metallization process is used to form ohmic contacts and interconnections by physical or chemical vapour deposition. This process deposits a conductive thin film over the semiconductor surface, followed by photolithography to define the front contacts and other patterning purposes [26].

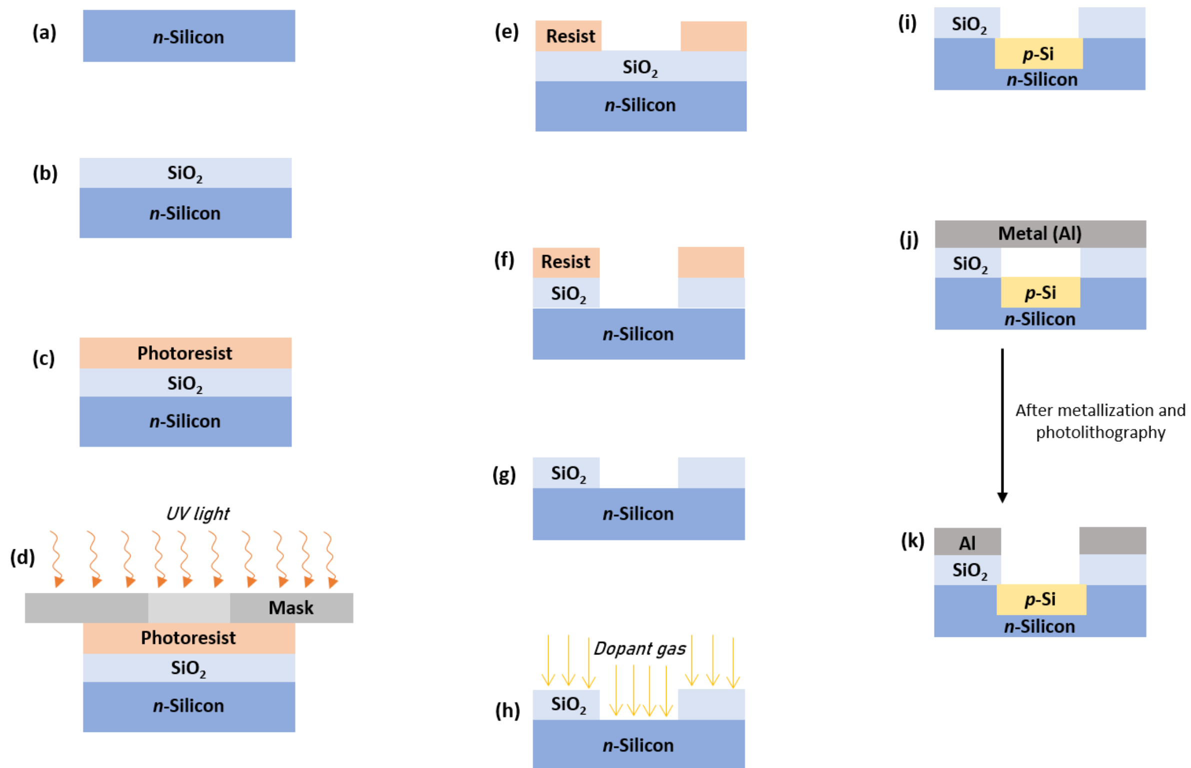

Fig. 4 - Overall fabrication processes of a typical *p-n* junction diode

2. Methodology

2.1 Design and Simulation of Fabrication Processes

The main software used to design and simulate the fabrication processes of the diode was the IntelliSuite software, and AutoCAD was also used in designing mask patterns for photolithography. Once the virtual fabrication processes were successfully verified, physical fabrication was carried out. Based on the characterization and analyses of the fabricated diodes, the fabrication processes were modified to get best-performing devices.

Using the IntelliSuite software involved two parts; IntelliMask for designing and exporting masks, and IntelliFab for verification and virtual analysis of fabrication processes that could be used as reference for practical works. Three layers of masks were designed using IntelliMask; mask 1 was designed to pattern SiO_2 layer that forms a window for thermal diffusion of phosphorus onto *p*-type silicon wafer, mask 2 was designed to form SiO_2 barrier on the substrate and mask 3 was designed for deposition of four aluminium (Al) metal contacts (Figure 5). The overall fabrication processes designed in IntelliFab software is shown in Figure 6.

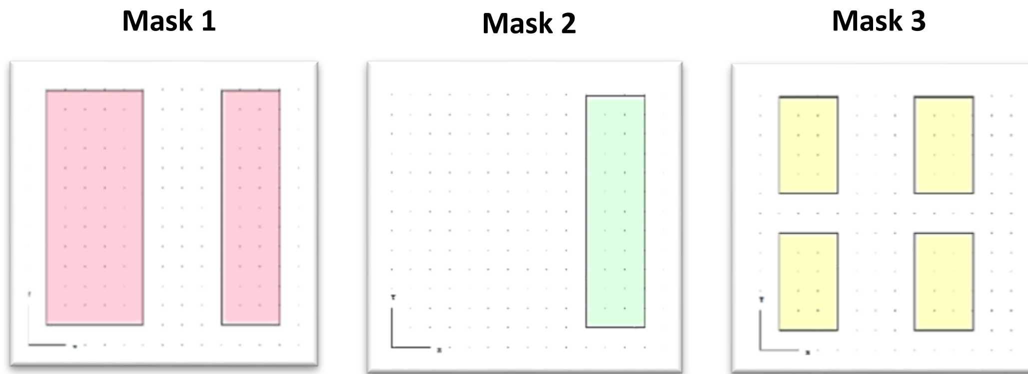

Fig. 5 - Mask designs for fabrication processes, modeled using IntelliMask software

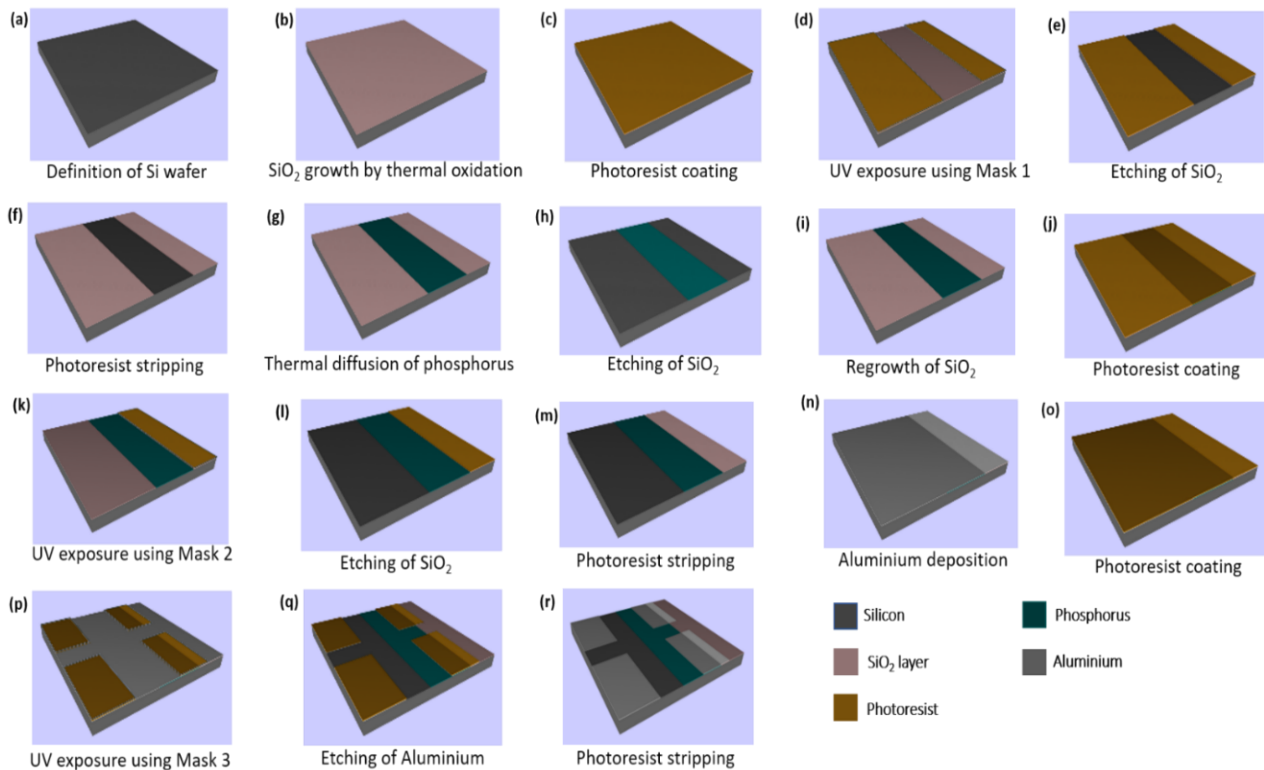

Fig. 6 - Simulation of fabrication processes designed with IntelliFab software

AutoCAD software was used to design duplicates of mask patterns, in smaller (mm) dimensions, for photolithography. This was done to fit several sensors one a 4-inch (100 mm) silicon wafer. Figure 7 shows all three mask designs with varying dimensions on a silicon wafer. These designs were then printed on transparent masks by using laser jet printer. The white regions on the design represent the region that will not be penetrated upon exposure of UV light during photolithography, and they were printed in black on the transparent masks.

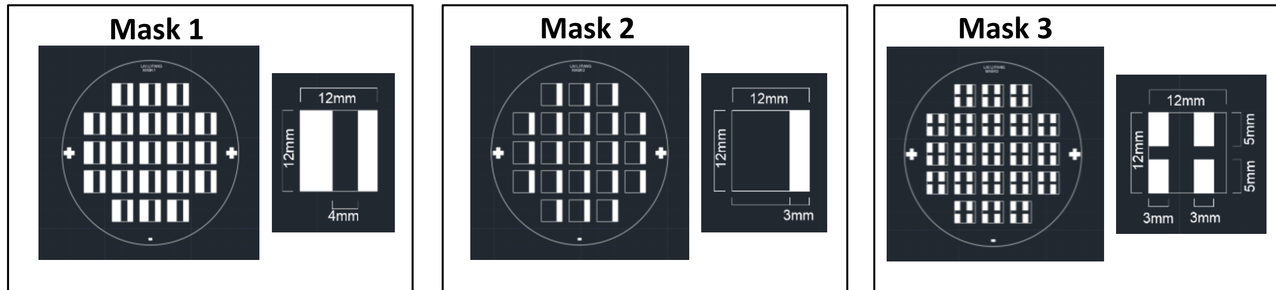

Fig. 7 - Mask designs on silicon wafer, modeled using AutoCAD software

2.2 Fabrication of *p-n* Diodes

In this study, *p*-type silicon wafers were used. The overall fabrication processes are as described in Figure 8. The wafer surface was pre-cleaned using buffered oxide etchant (BOE) solution for 20 seconds, followed by rinsing with deionized (DI) water and drying of the wafers with nitrogen gun.

Next, the wafers underwent thermal oxidation for growth of SiO_2 layer. The oxidation furnace was pre-set to heat to 600 ^{0}C in nitrogen atmosphere for the ramp up process. Once the temperature reached 600 ^{0}C, the wafers were loaded into the furnace and the temperature was increased to 1000 ^{0}C. Oxygen gas was introduced into the furnace *via* water heater after the temperature was stabilized, and the nitrogen source was also switched off. This oxidation process was carried out for 1 hour, and afterwards the temperature was set to 300 ^{0}C for ramp down process and finally the wafers were removed from the furnace to be cooled to room temperature.

For photoresist coating, positive photoresist (PR1-2000A) was spin-coated on the oxidized wafers. Around 5 mL of photoresist was dispensed on the wafer, and was spun with these settings consecutively and continuously; 1000 rpm for 5 seconds, 3000 rpm for 10 seconds, and 1000 rpm for 15 seconds. This was to ensure the even coating of the photoresist. The wafers were then soft baked on a hot plate at 90 ^{0}C for 90 seconds to remove excess moisture from the photoresist. To start of the photolithography, the transparent mask 1 was properly placed and aligned on the wafer, and was exposed to UV light for 110 seconds. This exposed wafer was immersed into an RD-6 developer solution for around 40 seconds, then the developed wafer was rinsed with DI water and spun dry. Then, etching process was carried out by immersing the wafer in BOE solution for 2 minutes to remove oxide layer from the undeveloped region, and the now-patterned wafer was rinsed with DI water and spun dry. Finally, the wafer was rinsed with acetone to remove all photoresist from the wafer, followed by rinsing with DI water and spin drying.

Thermal diffusion for impurity doping was carried out in an *n*-type diffusion furnace, and phosphorus was used as the *n*-type dopant. The diffusion furnace was set to heat to 600 ^{0}C for ramp up process, meanwhile the samples were prepared by placing a phosphorus solid planar source in between the sample wafers in a wafer boat. After the temperature reached 600 ^{0}C, the wafer boat was loaded into the furnace and the temperature was increased to 1000 ^{0}C with nitrogen-to-oxygen gas ratio of 4:1. The nitrogen gas removed air contaminants from the furnace, and allowed dopant vapour to flow through a concentration gradient. Once the temperature hit 1000 ^{0}C, the nitrogen-to-oxygen gas ratio was adjusted to 10:0, and the diffusion process was carried out for 1 hour. After diffusion, the nitrogen-to-oxygen gas ratio was re-adjusted to 0:10 for stabilization purposes, and the furnace temperature was decreased to 300 ^{0}C. The wafers were loaded out of the furnace and cooled to room temperature.

The thermal oxidation and photolithography processes were repeated using mask 2, and afterwards metallization process was carried out using mask 3. Physical vapour deposition (PVD) method was employed, and aluminium was used as the contacts of the diodes. This metallization process was done with a certain protocol, and the equipment settings are summarised in Figure 8. After aluminium deposition, photolithography was done for contacts definition (using mask 3) and an aluminium etcher was used to remove aluminium within the undeveloped region.

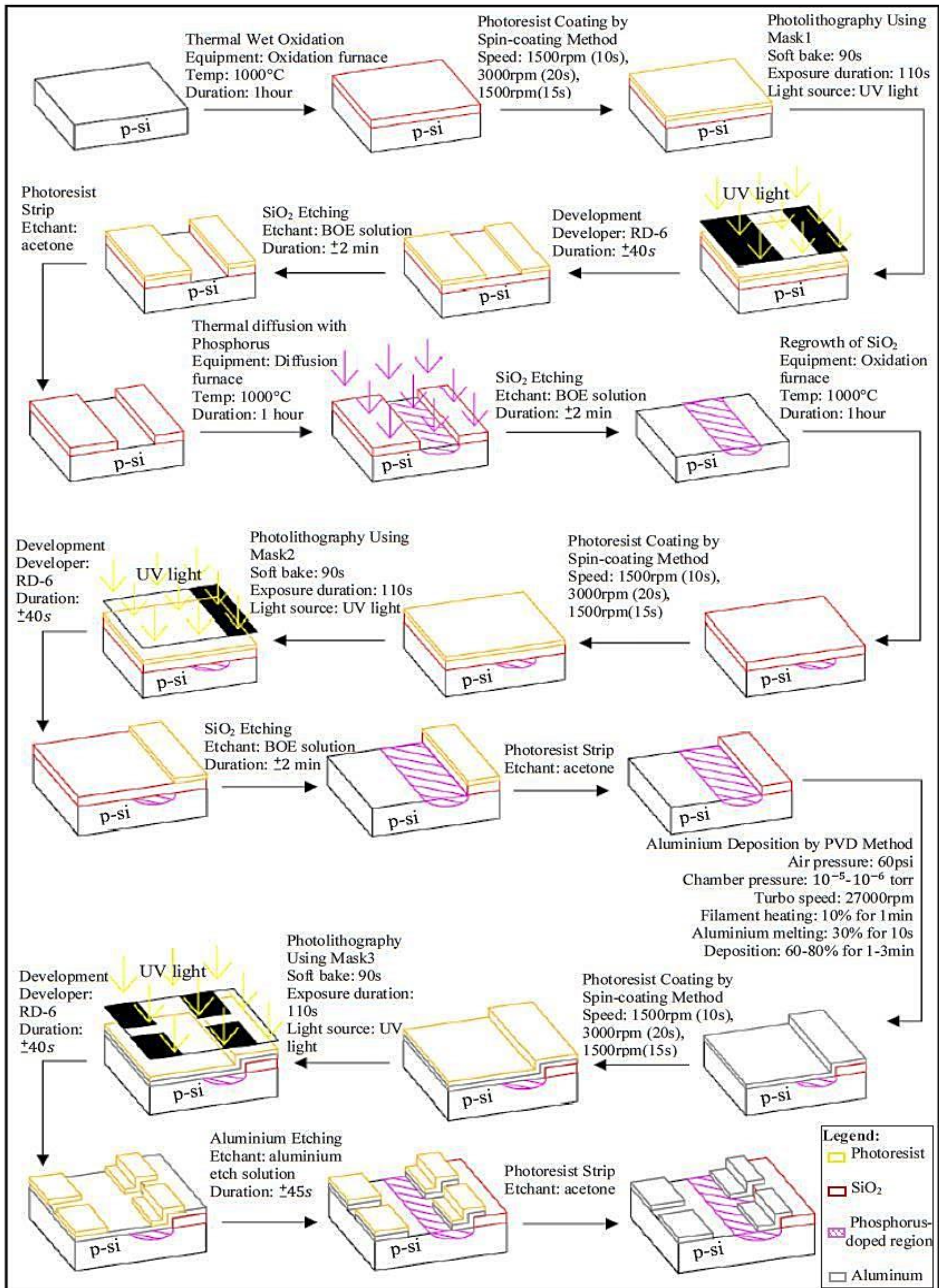

Fig. 8 - Overall fabrication process flow of diode sensor with detailed procedures

2.3 Four-point Probe Measurement

A four-point probe was used to measure the resistivity as well as sheet resistivity of the top emitter layer experimentally. The four equally spaced probes are brought in contact with a material of unknown resistance. A current is supply and flow through the outer probes and the inducing voltage in inner probes is measured. The relationship of the current and voltage values is dependent on the resistance of the space between the probes and the resistivity of the material. The sheet resistance and resistivity were calculated using equation (3) and (4). All experiments were repeated three times. The mean ($\bar{x}$) and standard deviations (SD) of the three repeat of measurements were calculated by:-

$$\bar{x} = \frac{(\sum x)}{n} \quad (3)$$

$$SD = \sqrt{\frac{\sum(x-\bar{x})^2}{n-1}} \quad (4)$$

where x is the measured value and n is the number of samples.

3. Results & Discussion

3.1 Physical Characteristics

The fabricated diode sensors were inspected using water contact angle measurement and Raman spectroscopy to determine the physical characteristics. Contact angle measurement was done to determine the hydrophobicity of the diode surface [28]. or this measurement, the water droplet was dropped on the channel of the diode, which was in between the *p-n* junction. Four measurements were done on both *p* and *n* regions, and the total average contact angles for the positive (silicon) region and negative (phosphorus-doped) region were 103.9°±2.0 and 101.75°±1.6 respectively. Both regions had contact angles larger than 90°, indicating that the *p-n* junction surface was hydrophobic [29]. Note that the negative region is slightly less hydrophobic that the positive region, this is due to the doping of phosphorus, which is hydrophilic in nature.

Raman spectroscopy was used to analyse the composition of the diode, specifically the *p-n* junction surface. Raman spectrum of bare silicon wafer was obtained, and a sharp peak appeared close to 520 cm^{-1}, indicating crystallization of the Si surface [28]. For the device, three regions were analysed; the positive region, the negative region and in between the *p-n* junction, and the Raman peaks were observed at 529 cm^{-1}, 523 cm^{-1} and 526 cm^{-1} respectively, shown in Figure 9. The Raman peak of *p-n* junction had the highest intensity, while Raman peak of negative region had the lowest intensity.

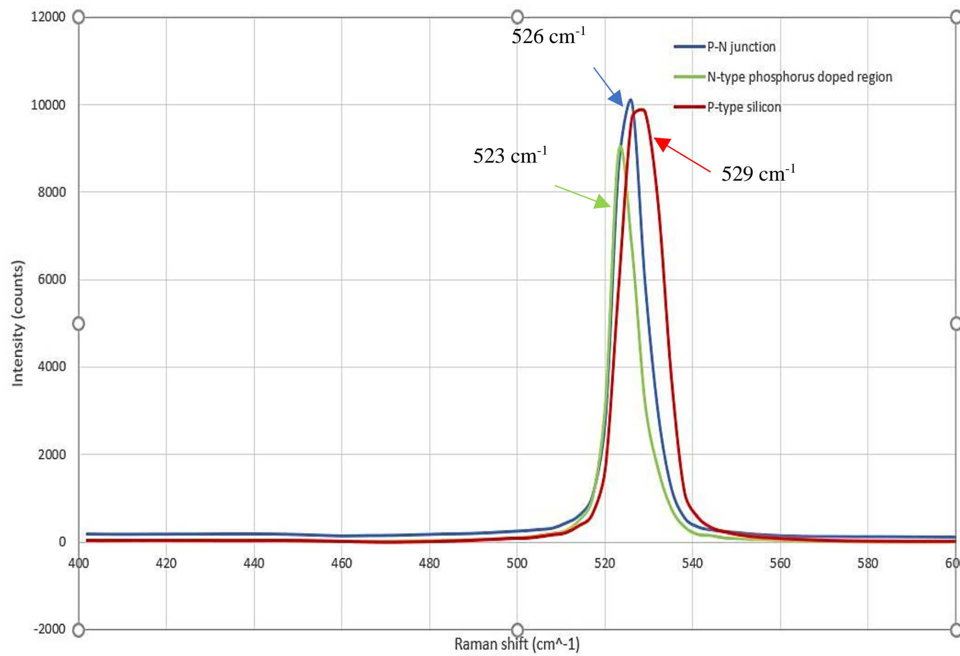

Fig. 9 - Raman spectra of p-region, n-region and *p-n* junction

By referring to a theory studied by Lee *et al.*, in silicon (un-doped and doped) films, a peak arising around 520 cm^{-1} can be assigned to the Si-Si longitudinal optical (LO) Raman peak, and when the silicon film is doped with phosphorus, the Si-Si LO Raman peak blue shifts to shorter wavelength [30]. The doping of phosphorus inside the silicon films induces a phonon shift in the first-order Si-Si LO vibration mode, depending on the concentration of phosphorus. As the phosphorus concentration increases, the intensity ratio of the Si-Si mode also increases, which can be explained in terms of the number of Si-P bonds in the silicon films with high phosphorus dopant concentration [30].

3.2 Electrical Characterization

The electrical properties of the diode sensors were analysed using four-point probe for sheet resistance (R_{sh}) and resistivity (ρ) and two-point probe for I-V measurement. The sheet resistance and resistivity of the fabricated wafer were taken from nine different mapping positions, and the average values of these parameters were calculated using Equations (1) & (2) respectively [25]. During the fabrication processes, the sheet resistance and resistivity of the oxidized SiO_2 film and phosophorus-doped silicon region were measured to determine the uniformity of these films. These results are summarized in Table 1.

Both average sheet resistance and resistivity values increase upon thermal oxidation of the silicon wafer, this is because the grown oxide layer acts as an insulating barrier. For thermal diffusion of phosphorus, the sheet resistance of the doped layer increase, but the resistivity of the layer decrease. The relationship between the sheet resistance and resistivity of a material is linearly proportional (based on equation (1)), hence it is expected that the sheet resistance increases as the resistivity increase. This anomaly however could be caused from problems during thermal diffusion process, where the phosphorus layer deposited is not uniform.

Table 1 - The average sheet resistance R_{sh} and resistivity ρ of diode using four-point probe

Parameters	Bare Si film		After oxidation (SiO_2 layer)		Phosphorus-doped Si layer	
	Mean	Standard Deviation	Mean	Standard Deviation	Mean	Standard Deviation
Sheet resistance, R_{sh} (Ω/sq)	1.45×10^2	0.04	3.00×10^4	0.50	3.50×10^5	0.66
Resistivity, ρ (Ω-cm)	5.45	0.16	1.11×10^3	1.83	3.05×10^1	0.50

For the I-V measurement using two-point probe, the voltage was fixed at a range between +12V to -12V. Figure 10(a) shows the I-V curve graph of two selected fabricated devices, Diode 1 & 2. The average knee voltage measured was 11.5 V and the average breakdown voltage was -4 V. The knee voltage is quite high, compared to bare silicon diode with knee voltage of 0.6V (AC), this is probably because of the wide channel length (*p-n* junction) of the diode, longer channel length contributes to higher knee (turn-on) voltage.

One sensor was then tested with different current limits (2, 6, 8, 10 mA), this was carried out to find the optimal functional voltage and current supply for the sensors.

Under forward bias condition, the curve graph rises exponentially, indicating the current flow through the device due to the diffusion of majority carrier [15]. At the reverse bias condition, the current remains nearly to zero. However, a sufficiently large negative voltage known as breakdown voltage will cause the diode to become conductive to negative current. Figure 10(b) at forward bias curve inset show that the I-V linear region has stepper current trend as compared to reverse bias inset. In the theory, the stepper current trend is due of the narrower depletion region on the forward bias region whereas, a wider depletion region in reverse bias. It can also be observed the curve achieved the saturation point at 11.5 V and breakdown voltage at -4 V. As shown in Figure 10(b), the linear region of I-V curve becomes steeper because of the decrease in resistivity with increasing current, implicated in equation (2).

The I-V characteristics of the diode sensor was also measured and compared under light and dark condition. This test was carried out to investigate the reliability of the sensor in different environments. Shown in Figure 10(c), the current flow of diode in reverse bias condition shows a steeper curve under both light and dark conditions compared to current flow in forward bias mode, this shows that the sensor is more sensitive at breakdown voltage compared to knee voltage. From these results, it can be concluded that this diode has the characteristics of a photodiode, in which a photodiode is always operated under reverse bias condition and is photosensitive [31].

Finally, the sensor was tested for salt detection. This salt detection experiment was carried out with different concentrations of salt solution (5 to 60 mg/mL) deposited on the *p-n* junction of the diode sensor. The salt contents for chips in the market is usually 8 mg per 100 mg of chips. Based on this nutritional fact, the experiment was carried out for testing 5 to 60 mg/mL of salt. The voltage supply was kept constant at a range between +12 to -12V, and this experiment was performed under normal light condition at room temperature. To prove this test reliable, four sensors were used and average values were calculated between these four measurements, shown in Figure 10(d). The current measurement starts to decline after 45 mg/mL, hence this is the maximum salt solution concentration that can be detected

by this diode sensor. The salt concentration in sweat is expected to be in the range of 460 to 1609 µg/mL [32], therefore this sensor can potentially be used to detect salt concentration in sweat.

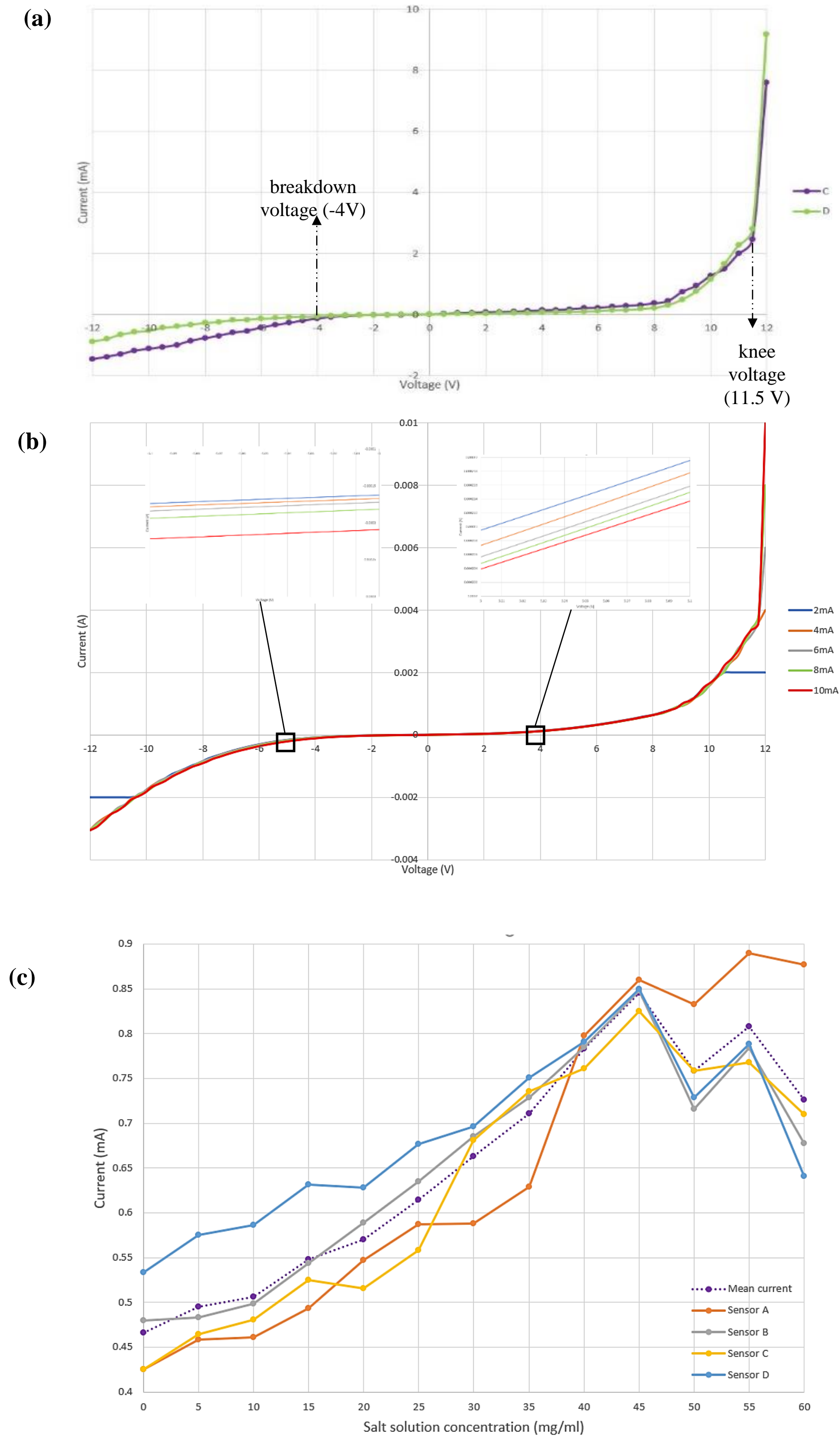

Fig. 10 - (a) I-V characteristics of fabricated diodes; (b) I-V characteristics of diodes under different current limits; (c) Current measurements of diode sensor upon salt detection

4. Conclusion

Diode-based sensors for salt solution detection were successfully designed and fabricated using planar fabrication technology, which included thermal oxidation, thermal diffusion, photolithography and metallization. The fabrication steps were simulated using IntelliSuite software, and designing of appropriate masks were done using both IntelliSuite and AutoCAD software. For electrical characterization, average sheet resistance and resistivity of the diode sensor were measured to be 3.50 x $10^5 \pm 0.66$ Ω⁄sq and 3.05 ± 0.5 Ωcm respectively. This sensor also showed ideal I-V diode characteristics, with knee voltage of 11.5V and breakdown voltage of -4 V. For salt concentration detection, the sensor successfully detected salt concentration changes with respect to current flow, and the maximum salt concentration that was detectable was until 45 mg/mL.

Acknowledgment

This research was funded by the Ministry of Higher Education Malaysia (MOHE). The authors would also like to acknowledge the research staff who provided frequent assistance during the course of this project.

References

[1] Grillo A., Salvi L., Coruzzi P., Parati G. (2019). Sodium intake and hypertension. Nutrients, 11, 1970
[2] Pirovano P., Dorrian M., Shinde A., Donohoe A., Brady A. J., Moyna N. M., Wallace G., Diamond D., McCaul M. (2020) A wearable sensor for the detection of sodium and potassium in human sweat during exercise. Talanta, 219, 121145
[3] Salvo P., Di Francesco F., Constanzo D., Ferrari C., Trivella M. G., De Rossi D. (2010). A wearable sensor for measuring sweat rate. IEEE Sensors Journal, 10, 1557-1558
[4] Parrilla M., Cuartero M., Crespo G. A. (2018). Wearable potentiometric ion sensors. Trends in Analytical Chemistry, 110, 303-320
[5] Choi D. H., Cutting G. R., Searson P. C. (2017). A wearble potentiometric sensor with integrated salt bridge for sweat chloride measurement. Sensors and Actuators B: Chemical, 250, 673-678
[6] Lee Y., Howe C., Mishra S., Lee D. S., Mahmood M., Piper M., Kim Y., Tieu K., Byun H. S., Coffey J. P., Shayan M., Chun Y., Constanzo R. M., Yeo W. H. (2018) Wireless, intraoral hybrid electronics for real-time quantification of sodium intake toward hypertension management. Proceedings of the National Academy of Sciences PNAS, 115, 5377-5382
[7] Choi D. H., Kim J. S., Cutting G. R., Searson P. C. (2016) Wearable potentiometric chloride sweat sensor: The critical role of the salt bridge. Analytical Chemistry, 88, 12241-12247
[8] Arakawa T., Kuroki Y., Nitta H., Chouhan P., Toma K., Sawada S., Takeuchi S., Sekita T., Akiyoshi K., Minakuchi S., Mitsubayashi K. (2015) Mouthguard biosensor with telemetry system for monitoring saliva glucose: A novel *cavitas* sensor. Biosensors and Bioelectronics, 84, 106-111
[9] Kim J., Valdes-Ramirez G., Bandodkar A. J., Jia W., Martinez A. G., Ramirez J., Mercier P., Wang J. (2014) Non-invasive mouthguard biosensor for continuous salivary monitoring of metabolites. Analyst, 139, 1632-1636
[10] Kim J., Imani S., de Araujo W. R., Warchall J., Valdes-Ramirez G., Paixao T. R.L.C., Mercier P.P., Wang J. (2015) Wearable salivary uric acid mouthguard biosensor with integrated wireless electronics. Biosensors and Bioelectronics, 74, 1061-1068
[11] Lee Y. H., Kweon O. Y., Yoo J. H., Han S. G., Oh J. H. (2018) Recent advances in organic sensors for health self-monitoring systems. Journal of Materials Chemistry C, 6, 8569-8612
[12] Chen Y. L., Kuan W. H., Liu C. L. (2020) Comparative study of the composition of sweat from eccrine and apocrine sweat glands during exercise and in heat. International Journal of Environmental Research and Public Health, 17, 3377
[13] Kraft T. M., Berger P. R., Lupo D. (2017) Printed and organic diodes: Devices, circuits and applications. Flexible and Printed Electronics, 2, 3
[14] Dixon A. E., Leslie J. D. (1979). Solar Energy Conversion: An Introductory Course. Amsterdam: Elsevier Ltd
[15] Fraser C. J., Smith E. H. (1994). Mechanical Engineer's Reference Book (12th ed.). Amsterdam: Elsevier Ltd
[16] Mishra U. K., Singh J. (2008). Semiconductor Device Physics and Design. (pp. 146-214) Netherlands: Springer.
[17] Ashby D. (2012) Electrical Engineering 101. (pp. 67-131). Amsterdam: Elesevier Inc
[18] Ding J., Qin W. (2020). Recent advances in potentiometric biosensors. Trend in Analytical Chemistry, 124, 115803
[19] Prudenziati M., Hormadaly J. (2012) Printed Films; Materials Science and Applications in Sensors, Electronics and Photonics, (pp. 366-409). Cambridge: Woodhead Publishing Ltd
[20] Mitsubayashi K., Niwa O., Ueno Y. (2019) Chemical, Gas, and Biosensors for Internet of Things and Related Applications, (pp. 147-160). Amsterdam: Elsevier Inc
[21] Cosio M. S., Scampicchio M., Benedetti S. (2012) Chemical Analysis of Food: Techniques and Applications, (pp. 219-247). Amsterdam: Elsevier Inc

[22] Fouletier J., Fabry P. (2003). Chemical and Biological Microsensors Application in Liquid Media, London: ISTE Ltd, 2010.
[23] Zhang J., Zhang H., Wu J., Zhang J. (2013). PEM Fuel Cell Testing and Diagnosis, (pp. 143-170). Amsterdam: Elsevier Inc
[24] Webster J. G. (1999). The Measurement, Instrumentation and Sensors Handbook, Germany: Springer
[25] Santos T. G. (2014). Surface Modification by Solid State Processing, (pp. 153-176). Cambridge: Woodhead Publishing Ltd
[26] May G. S., Sze S. M. (2003) Fundamentals of Semiconductor Fabrication, New Jersey: John Wiley & Sons
[27] Reinhardt K., Kern W. (2018) Handbook of Silicon Wafer Cleaning Technology (3rd ed.) Amsterdam: Elsevier Inc
[28] Bryk P., Korczeniewski E., Szymanski G. S., Kowalczyk P., Terpilowski K., Terzyk A. P. (2020) What is the value of water contact angle on silicon? Materials, 13, 1554
[29] Hebbar R. S., Isloor A. M., Ismail A. F. (2017) Membrane Characterization (pp. 219-255) Netherlands: Elsevier B.V
[30] Lee M., Ko E., Ko D. H. (2017) Probing lattice vibration and strain states in highly phosphorus-doped epitaxial Si films. Journal of Materials Chemistry C, 5, 9744-9752
[31] Harres D. (2013) MSP430-based Robot Applications. (pp. 273-298) Amsterdam: Elsevier Inc
[32] Montain S. J., Cheuvront S. N., Lukaski H. C. (2007) Sweat mineral-element responses during 7h of exercise-heat stress. International Journal of Sport Nutrition and Exercise Metabolism, 17, 574-582